

Assesment of zonal symmetric and asymmetric components of the Southern Annular Mode using a novel approach

Elio Campitelli * and Leandro Díaz

*Universidad de Buenos Aires, Facultad de Ciencias Exactas y Naturales, Departamento de
Ciencias de la Atmósfera y los Océanos, Buenos Aires, Argentina CONICET – Universidad de
Buenos Aires, Centro de Investigaciones del Mar y la Atmósfera (CIMA), Buenos Aires, Argentina
CNRS – IRD – CONICET – UBA, Instituto FrancoArgentino para el Estudio del Clima y sus
Impactos (UMI 3351 IFAECI), Buenos Aires, Argentina*

Carolina Vera

*Corresponding author: Elio Campitelli, elio.campitelli@cima.fcen.uba.ar

ABSTRACT

11 Enter the text of your abstract here. This is a sample American Meteorological Society (AMS)
12 L^AT_EX template. This document provides authors with instructions on the use of the AMS L^AT_EX tem-
13 plate. Authors should refer to the file amspaper.tex to review the actual L^AT_EX code used to create
14 this document. The template.tex file should be modified by authors for their own manuscript.

15 *Significance statement.* This is significant because I wrote it.

16 **1. Introduction**

17 The Southern Annular Mode (SAM) is the main mode of variability in the Southern Hemisphere
18 extratropical circulation (Rogers and van Loon 1982) in daily, monthly, and decadal timescales
19 (Baldwin 2001; Fogt and Bromwich 2006) and exerts an important influence in weather conditions
20 such as temperature and precipitation anomalies and sea ice concentration (Fogt and Marshall
21 2020). Its positive phase is traditionally described as anomalously low pressures over Antarctica
22 surrounded by a ring of anomalous high pressures in middle-to-high latitudes.

23 Most authors describe the SAM as a zonally symmetric pattern, a fact that is reflected not only
24 in its name, but also in the various methods used to characterise it. Of the several different
25 indices presented in the literature, many of them are based on zonal means of sea level pressure
26 or geopotential height (Ho et al. 2012). Gong and Wang (1999) defined the SAM index as the
27 zonal mean sea level pressure difference between 40°S and 60°S, which is also the definition used
28 by the station-based index in Marshall (2003). Baldwin and Thompson (2009) proposed defining
29 the Northern and Annular modes as the leading EOF of the zonally averaged geopotential height
30 at each level.

31 Even though these indices are based on zonal averages, the spatial the spatial structure of the
32 SAM computed from them contains noticeable deviations from zonal symmetry, particularly in the
33 Pacific Ocean region. These zonal asymmetries have not been widely studied, but previous work
34 suggest that they strongly modulate the regional impacts of the SAM, going as far as reversing
35 its relationship between precipitation in South America (Silvestri and Vera 2009). At the very
36 least, the fact that the SAM is not entirely zonally symmetric hinders our ability to reconstruct

37 its historical variability prior to the availability of dense observations in the Southern Hemisphere
38 (Jones et al. 2009).

39 At least some of the variability associated with the zonal asymmetries of the SAM is probably
40 forced by the tropics. In particular, ENSO-like variability affects the Southern Hemisphere ex-
41 tratropics through the Pacific-South American Pattern (Mo and Ghil 1987; Kidson 1988; Karoly
42 1989), whose wave train projects strongly onto the zonal anomalies corresponding to the SAM
43 in the Pacific sector. And although the relationship between ENSO and SAM is far from simple,
44 tropical influences on the SAM have been observed (Fan 2007; Fogt et al. 2011; Clem and Fogt
45 2013).

46 Positive trends in SAM index have been documented by various researchers using different
47 indices mostly on boreal Summer and Autumn (Fogt and Marshall 2020, and references therein).
48 These trends are thought of driven primarily by stratospheric ozone depletion and understood in
49 the context of zonal mean variables. However, it's not clear how or if the asymmetric component
50 responds to this forcing, or whether its variability could be masking influencing the observed trends
51 independently.

52 Similarly unclear are the specific impacts of the zonally asymmetric component of the SAM.
53 Positive phase of the SAM is associated with generally colder temperatures over Antarctica and
54 warmer temperatures at higher latitudes (Jones et al. 2019) (and viceversa for negative SAM), but
55 there are significant deviations from this zonal mean response, notably in the Antarctic Peninsula
56 and the South Atlantic (Fogt et al. 2012). The SAM signal in precipitation behaves similarly,
57 although with even greater deviation from zonal symmetry (Lim et al. 2016). The importance of
58 zonal asymmetries of the SAM in these impacts have been studied in certain regions. For example,
59 the SAM-precipitation relationship in Southeastern South America and Southern Brazil can be
60 explained by the PSA-like zonally asymmetric circulation associated with the SAM (Rosso et al.

61 2018). Fan (2007) also found that precipitation in East Asia was impacted by the variability of only
62 the Western Hemisphere part of the SAM.

63 We are not aware of any previous work which quantifies the temporal variability of the asymmetric
64 component of the SAM with the exception of Fogt et al. (2012). However, their methods based
65 on composites of positive and negative SAM events leads to some issues, such as spatial patterns
66 derived from as little as 4 cases and from imbalanced periods (for example, 5 of the 7 cases in
67 their DJF SAM+ composite are from later than 1988, whereas all of the 8 years in their DJF SAM-
68 composite are from earlier than 1988). This is particularly important due to the inhomogeneities
69 in reanalysis products prior to the satellite era and the possible change in the asymmetric structure
70 of the SAM (Silvestri and Vera 2009).

71 Moreover, Fogt et al. (2012) studied the zonal asymmetric component of the SAM only in sea
72 level pressure. Zonal asymmetries in the SAM spatial pattern are fairly barotropic throughout the
73 troposphere, but they change dramatically in the stratosphere (Baldwin and Thompson 2009).

74 Our objective is, then, to systematically characterise the zonally asymmetric and symmetric
75 components of the SAM variability. For each level, we construct two indices which aim to
76 capture exclusively the variability of the symmetric and asymmetric component respectively. We
77 assess their vertical structure and coherence, temporal variability and trends. We then study the
78 spatial patterns described by the variability exclusive to each index. Finally, we investigate their
79 relationship with temperature and precipitation anomalies.

80 In the Section 2 we describe the methods. In Section 3.a we describe the temporal variability
81 and vertical coherence of the indices. In Section 3.b, we analyse the spatial patterns of geopo-
82 tential height associated with them. In Section 3.c, we study their relationship with surface-level
83 temperature and precipitation.

2. Methods

sec:methods

1) DATA

To describe the Southern Annular Mode and its variability we used monthly geopotential height at 2.5° longitude by 2.5° latitude of horizontal resolution and 37 vertical isobaric levels from ERA5 (Hersbach et al. 2020) for the period 1979 to 2018. We restrict our analysis to the post-satellite era to avoid any confounding factors arising from the introduction of satellite observations.

We describe the relationship between the SAM indices and temperature and precipitation. We use temperature data from NOAA's Merged Land Ocean Global Surface Temperature Analysis V4.0.1 (Vose et al. 2012; Smith et al. 2008), which blends land and ocean temperature analysis into a monthly global grid 5° longitude by 5° latitude. For precipitation, we use monthly, 0.5° longitude by 0.5° latitude data from the Global Precipitation Climatology Centre (Schneider et al. 2015).

2) DEFINITION OF INDICES

Traditionally the Southern Annular Mode (SAM) is defined as the leading Empirical Orthogonal Mode (EOF) of sea level pressure or geopotential height at lower levels (Ho et al. 2012). Following Baldwin and Dunkerton (2001), we extend that definition vertically and use the term SAM to refer to the leading EOF of the monthly anomalies of geopotential field south of 20°S at each level. We performed EOFs by computing the Singular Value Decomposition of the data matrix consisting in 481 rows and 4176 columns (144 points of longitude and 29 points of latitude). We weighted the values by the square root of the cosine of latitude to account for the non-equal area of each gridpoint (Chung and Nigam 1999).

To separate between the zonally symmetric and asymmetric components of the SAM, we computed the zonal mean and anomalies of the full SAM spatial pattern, as shown in Figure 1 for 700hPa. The full spatial signal ($\text{EOF}_1(\lambda, \phi)$) is the sum of the zonally asymmetric ($\text{EOF}_1^*(\lambda, \phi)$)

and symmetric ($[EOF_1](\lambda, \phi)$) components. We then compute the “Full SAM”, “Asymmetric SAM” and “Symmetric SAM” indices as the regression coefficients of the regression of each monthly geopotential field on the respective patterns (weighting by the cosine of latitude). The three indices are normalised by dividing them by the standard deviation of the “Full” index at each level. As a result, the magnitude between indices is comparable. However, only “Full” index will have unit standard deviation per definition. From the regression, we also use the explained variance of each pattern as a indication of the degree of symmetry or asymmetry of each monthly field.

Our method assumes linearity in the asymmetric component of the SAM. That is, we assume that zonal symmetries associated with positive SAM are opposite and equal to the ones associated with negative SAM. Fogt et al. (2012)’s composites (their Figure 4) suggest that this might not be entirely valid, although we argue that much of that apparent non-linearity is due to the heterogeneous nature of the selected years for constructing the composites. Using our data (from 1979 to 2018), seasonal composites of zonal anomalies of 700 hPa geopotential height for SAM+ (Full SAM index greater than 1 standard deviation) and SAM- (smaller than negative 1 standard deviation) show relatively high pattern correlations all seasons and are visually very linear (Figure A9). Therefore, we believe that our method is at the very least a reasonable approximation of the phenomenon.

By computing a single EOF pattern using data for all months we are assuming that the zonal anomalies of the SAM are the same in all seasons. Geopotential zonal anomalies computed by projecting the first EOF of *each season* are very similar to each other (Figure A10) and show pattern correlations between 0.65 (DJF with JJA) and 0.9 (between MAM and SON). Based on this, we believe that our initial assumption is not unreasonable.

Finally, we assume that the zonally asymmetric pattern is stationary in time. Silvestri and Vera (2009) suggest that this might not be the case between 1958 and 2004 but the period we analyse is much shorter (1979-2018) so it’s unlikely that we could observe significant changes. Moreover,

131 zonal asymmetry of the spatial patterns for the two halves of the period (1979 to 1998 and 1999 to
132 2018) show no systematic change (Figure A11).

133 3) REGRESSIONS

134 We perform linear regression to quantify the association between the SAM indices and other
135 variables. Since the Asymmetric and Symmetric SAM indices are significantly correlated with
136 each other, to capture the variability explained uniquely by each index we use one multiple linear
137 regression instead of two simple linear regressions. To obtain the linear coefficients of a variable
138 X (geopotential, temperature, precipitation, etc. . .) with the Asymmetric SAM (SAM_a) and
139 Symmetric SAM (SAM_s) we fit the equation

$$X(\lambda, \phi, t) = \alpha(\lambda, \phi)SAM_a + \beta(\lambda, \phi)SAM_s + X_0(\lambda, \phi) + \epsilon(\lambda, \phi, t)$$

140 where λ and ϕ are the longitude and latitude, t is the time, α and β are the linear coefficients, X_0
141 and ϵ are the constant and error terms. From this equation, α represents the (linear) association
142 of X with the variability of the Asymmetric SAM that is not explained by the variability of
143 the Symmetric SAM; in other words, it is proportional to the partial correlation of X and the
144 Asymmetric SAM, controlling for the effect of the Symmetric SAM and viceversa for β .

145 At 2.5° by 2.5° resolution, a single regression field is composed of thousands of regressions. In
146 such case, using naive p-values to test for significance leads to misleading results (Walker 1914;
147 Katz and Brown 1991). While there are multiple proposed solutions in the literature, Wilks
148 (2016) suggests that adjusting p-values by controlling for the False Discovery Rate (Benjamini
149 and Hochberg 1995) is a simple and effective method to ameliorate this issue. Therefore, p-values
150 showed in regression fields are all adjusted following Benjamini and Hochberg (1995).

When performing a separate regression for each trimester (DJF, MAM, JJA, SON) we first average the relevant variables to obtain a single value for each year and each trimester.

3. Results

sec:results

a. Temporal evolution

sec:temporal

The temporal evolution of the Asymmetric and Symmetric SAM was firstly assessed. Figure 2 shows the corresponding time series for 700 hPa and 50 hPa and their corresponding density estimates. We selected these two levels as representative of the tropospheric and stratospheric variability respectively. As will be shown later, both indices are highly coherent within each atmospheric layer, therefore is reasonable to take one level as representative of each layer.

Month-to-month variability is evident for both indices, with noisy variations in the low frequency. At first glance the series can be distinguished by their distributions. Compared to the stratospheric indices, the stratospheric indices are much more long-tailed; that is, extreme values (both negative and positive) abound. The Asymmetric series have both more variability in the higher frequencies than the Symmetric series.

The stratospheric Symmetric SAM varies strongly with a two-year period, which can be seen by spectral analysis (Figure A3). This might suggest a link between stratospheric SAM variability and QBO. There is a local peak at 2 years in the periodogram of the tropospheric Symmetric SAM also, although it's not statistically significant. In the troposphere the most significant peak of variability is found in the Asymmetric index at around 3.6 months.

From Figure 2 we can see that the Asymmetric and Symmetric time series appear to be correlated. Moreover, looking at the extremes in the stratosphere, the Symmetric series appears to lag the Asymmetric series (see, for example, the positive events on late 1987). We show these correlations,

173 across all the levels of the reanalysis for zero and -1 lag (Asymmetric index leading the Symmetric
174 index), in Figure 3. Zero-lag correlations between the Asymmetric and Symmetric series are
175 relatively constant through the troposphere, fluctuating between 0.39 and 0.45. One-month-lag
176 correlations are similarly constant but significantly reduced to around 0.17. In the stratosphere,
177 zero-lag correlations drop to a minimum of 0.21 at 20 hPa and then it increases again monotonically
178 with height up to the uppermost level of the reanalysis (although results near the top of the models
179 are to be interpreted with care). At the same time, one-month-lag correlations increase with height.
180 As a consequence, stratospheric Symmetric index tends to precede corresponding Asymmetric index.

181 Figure 4a shows (zero-lag) cross-correlation across levels for the Full, Symmetric and Asym-
182 metric SAM indices. For the Full SAM (panel a), high values below 100 hPa reflect the vertical
183 (zero-lag) coherency throughout the troposphere. Above 100 hPa correlation between levels falls off
184 more rapidly, indicating less coherent (zero-lag) variability. Therefore, there is a non negligible
185 correlation between the troposphere and the lower-to-middle stratosphere. Examining panels b and
186 c, we see that the Asymmetric and Symmetric SAM share the same high level of coherency in the
187 troposphere but they differ in their stratospheric behaviour. Stratospheric coherency is stronger
188 for the Asymmetric SAM than the Symmetric SAM. The stratospheric Symmetric SAM seems to
189 connect more strongly to the troposphere than the Asymmetric SAM.

190 The trends for each of the indices (Full, Symmetric, Asymmetric) were evaluated for the whole
191 period 1979-2018 at each level (Figure 5) for the whole year and separated by trimesters. The Full
192 SAM index presents a statistically significant trend (panel a.1) that extends through the troposphere
193 up to about 50 hPa and reaches its maximum value at 100 hPa. The seasonal trends (rest of column
194 a) indicate that positive trends are present in Autumn and particularly in Summer, where the 100
195 hPa maximum is much more defined. Positive trends have been documented by previous studies

(e.g. Fogt and Marshall 2020, and references therein) using indices of the SAM based on surface or near-surface circulation.

By separating the SAM signal in its Asymmetric and Symmetric parts, we can not only see that these trends are almost entirely due to the Symmetric component (column b vs. column c), but in some cases the trends become more clear. In Summer, the Asymmetric SAM has a statistically non significant negative trend in the middle troposphere that obscures the trend in the Full index; as a result, trends computed using only the Symmetric component are more clear (compare the shading region in panel a.2 and c.2). In Autumn, using the Symmetric SAM reveals a statistically significant positive trend in the stratosphere that is not significant using the Full index.

We stress that these are only linear trends during the whole period and the absence of a statistically significant signal should not be taken as evidence of no systematic change. In particular, going back to Figure 2, we can see an evident change in the stratospheric Asymmetric component (red line in panel a) between the 90's, when we see a dominance of extreme negative values, and the 00's, when we see the inverse. This change is restricted to the Winter months: the linear trend for JJA starting in 1990 for the Asymmetric component at 50hPa is 0.37 ± 0.22 .

Figure 6 shows decadal trends for the explained variance of each index. There is no evidence of a significant trend in the stratosphere. In the troposphere, there is a positive trend for the Asymmetric SAM and no significant trend for the Symmetric SAM. This suggests that the SAM has become more asymmetric in the period from 1979 to 2018. The change is slight, though; of the order of 1% increased explained variance per decade.

b. Spatial patterns

sec:spatial

To show if, and to what extent, the Asymmetric and Symmetric SAM indices indeed capture the asymmetric and symmetric component of the SAM respectively, we computed the spatial

219 regression of geopotential height anomalies on these indices and the Full SAM index. Figure 7
220 shows these regressions. Regression coefficients in column a are computed using the Full SAM.
221 Regression coefficients in columns b and c are computed using multiple regression using the
222 Asymmetric and Symmetric indices at the same time. Thus, they are to be interpreted as the
223 patterns associated with each index, removing the variability (linearly) explained by the other
224 index.

225 In the stratosphere, the spatial pattern associated with the Full SAM is more clearly dominated by a
226 zonally symmetric, monopolar structure (panel a.1) which is, however, not perfectly centered in the
227 South Pole. The monopole obtained by multiple regression with the Asymmetric and Symmetric
228 SAM (panel c.1) is much more symmetric and the shift from total symmetry is captured by the
229 regression pattern of the Asymmetric SAM as a wave-1 with maximum anomalies above the
230 Belinghausen Sea on the Western Hemisphere and Davids Sea in the Eastern Hemisphere
231 (panel b.1).

232 In the troposphere, panel a.2 shows the well known combination of zonally symmetrical annular
233 mode with zonal asymmetries in the form of a wave-3. The regression using the Asymmetric and
234 Symmetric SAM indices successfully disentangle both structures. The Asymmetric component
235 gives rise to a cleaner zonal wave (panel b.2) and the Symmetric component is associated with an
236 trully annular mode, almost devoid of zonal asymmetries (panel c.2). The wave-3 pattern observed
237 in panel b.2 is rotated by half a wavelength from the average position of the mean wave-3 pattern
238 asociated with Raphael (2004)'s ZW3 index, whose reference locations are marked with points in
239 the figure. Thus, the tropospheric Asymmetric SAM index represents a zonal displacement in the
240 position of the climatological wave-3 pattern.

241 The amplitude of first zonal wave numbers at each latitude at 50 hPa and 700 hPa is shown in
242 Figure 8, where wave number zero represents the amplitude of the zonal mean. Column b shows

243 that the Asymmetric SAM is overwhelmingly dominated by wave 1 in the stratosphere (panel b),
244 while in the troposphere it is composed of zonal waves 3 to 1 in decreasing level of importance
245 (panel b). Looking at panel b.2 from Figure 7, it becomes apparent that zonal wavess 1 and 2
246 modulate the amplitude of zonal wave 3, which –as mentioned before– is larger in the Western
247 Hemisphere than in the Easten Hemisphere.

248 To analyse the vertical structure of the geopotential anomalies asociated with the asymmetric
249 SAM index, we show a vertical cross section of regressions of mean geopotential height between
250 65°S and 40°S for the 50 hPa Asymmetric SAM index (panel a) and for the 700 hPa Asymmetric
251 SAM index (panel b) (Figure 9). The geopotential anomalies associated with the stratospheric
252 Asymmetric SAM (panel a) are clearly constrained to the stratosphere, which underscores the
253 uncoupling between the stratospheric and tropospheric Asymmetric SAM. The vertical structure
254 of this signal tilts about 60°to the West between 100 hPa and 1 hPa, suggesting baroclinic processes.
255 Interestingly, the signal in the stratosphere maximises near 10 hPa despite using the 50 hPa index
256 for the regression.

257 The tropospheric Asymmetric SAM (panel b) has significant signals that extend upwards to the
258 uppermost levels of the reanalysis. In the troposphere, the wave-3 structure is equivalent barotropic
259 with maximum amplitude at roughly 250 hPa. The anomalies are much more intense in the Western
260 hemisphere, where they extent into the stratosphere. In the Eastern hemisphere the wave-3 signal
261 is weaker and confined to the troosphere while negative anomalies dominate in the stratosphere.
262 So, while the tropospheric Asymmetric SAM index is associated with stratospheric geopotential
263 anomalies, these do not project strongly onto the stratospheric Asymmetric SAM.

264 The structures shown in panels a and b in Figure 9 are surprisignly robust to the choice of index
265 level. For any stratospheric (above 100 hPa) index, the resulting anomalies are very similar to the

266 wave-1 structure with maximum near 10 hPa in panel a. Conversely, for any tropospheric (below
267 100 hPa) index, the result is very similar to panel b. The patterns mainly change in amplitude.

268 The wave-3 pattern from Figure 7 panel b.2 is very similar to the Pacific-South American Pattern
269 (Mo and Ghil 1987; Kidson 1988) which is a teleconnection pattern associated with the ENSO
270 (Karoly 1989). Indeed, Fogt et al. (2011) showed that there is a significant relationship between
271 the SAM and the ENSO. The correlation between the full SAM and the ENSO as measured by
272 the Oceanic Niño Index (Bamston et al. 1997) (ONI) is -0.16. Consistent with Fan (2007), we
273 show that this relationship is captured entirely the Asymmetric SAM, as this index has a partial
274 correlation of -0.26 with the ONI controlling for the effect of the Symmetric SAM, whereas the
275 Symmetric SAM's partial correlation with the ONI is essentially null (0.019). We performed
276 the same analysis using the Multivariate Enso Index (Wolter and Timlin 2011) and the Southern
277 Oscillation Index (Ropelewski and Jones 1987) to conclude that these results do not depend on the
278 ENSO index used.

279 *c. Impacts*

sec:impacts

280 The SAM has been shown to be associated with important surface variables such as temperature
281 and precipitation (e.g. Gillett et al. 2006, and see Fogt and Marshall (2020) for a review). Naturally,
282 most studies on the surface impacts of the SAM are based on an index identical or analogous to
283 what we call Full SAM index (Fogt et al. (2012) being the only exception that we are aware of).
284 We regress surface temperature and precipitation onto each of the three SAM indices to see if there
285 are different surface impact associated with the asymmetric and symmetric SAM circulation.

286 Figure 10 shows regression coefficients of each index at 700 hPa with surface temperature for
287 each trimester. In Summer positive values of the Full SAM index (panel a.1) are associated
288 with negative temperature anomalies near Antarctica which are surrounded by a ring of positive

anomalies. The ring is not zonally symmetric, as there are three clear local maximums around 30°W, 15°E and 50°E and a local minimum (with negative sign) around 120°W. In the tropics, there are negative anomalies in the equatorial Pacific, consistent with the negative correlation between SAM and ENSO. Panels b.1 and c.1 show temperature anomalies associated with positive values of the Asymmetric and Symmetric SAM, respectively. Both the local maximums in the ring and the anomalies in the Pacific regions are present mostly on the Asymmetric SAM regression map, while temperature patterns linked to positive Symmetric SAM show a more zonally consistent ring and less relation to the tropics. Noticeable, temperature anomalies in the Indian ocean, South Africa and Australia are strongly related to positive values of Asymmetric SAM. This signal is not present in the regression pattern with the Full SAM. Spring (row 4) features very similar patterns but of generally smaller in magnitude and statistical significance.

In Autumn and Winter (rows 2 and 3) the positive ring is only present through its local maximums in the regression with the Full SAM. There are also negative anomalies in Southern Australia, and positive anomalies over New Zealand and Southern South America. These patterns are not significant in the sense that there are no areas with p-values below 0.05 when controlling for FDR following Wilks (2016). However, repeating this analysis with 2-meter temperature from ERA5 resulted in similar patterns that were statistically significant. Moreover, similar features were observed in station measurements by Jones et al. (2019), although using data from 1957 to 2016.

The pattern of negative anomalies in the pole surrounded by positive anomalies roughly seen in all seasons –although with varying intensity and small-scale details– is consistent with the intensification and poleward migration of the westerlies commonly linked to the SAM. It's then not surprising to see it more clearly in association with the Symmetric SAM (at least in Summer and Spring).

312 These results suggests that Asymmetric and Symmetric SAM indices are associated with overall
313 distinct temperature patterns which may not be apparent when using the Full SAM index.

314 Figure 10 column b can be partially compared with Figure 11 from Fogt et al. (2012). Although
315 they used station data from 1958 to 2001, a lot of the characteristics are reproduced here, such as
316 the strong signal in New Zealand and Australia in Summer and Spring.

317 Regression of the SAM indices with seasonal mean precipitation and 700 hPa geopotential
318 height are shown Figures 11 and 12 for Australasia and South America respectively. South Africa
319 is not shown because no significant signal was detected there.

320 In Australia, the annual regression shows that the Full SAM index is positively associated with
321 precipitation in the Southeastern region (Figure 11 panel a.1), which reproduces the results from
322 Gillett et al. (2006). The separation between Asymmetric and Symmetric SAM suggest that
323 this positive anomaly is explained by the Symmetric SAM only in the East coast (panel c.1).
324 Geopotential anomalies associated with this index (black contours) are indicative of easterly flow
325 from the Tasman Sea, which could explain the positive anomalies in precipitation as found by
326 Hendon et al. (2007). The Asymmetric SAM appears related to increased precipitation in the West
327 coast of Southeastern Australia (panel b.2), which could similarly be explained by the anomalous
328 westerly circulation transporting moist air to the continent from the Indian Ocean.

329 This Spring signal is broadly consistent with Hendon et al. (2007), but whereas Hendon et al.
330 (2007) also detected a strong signal in Summer, panel a.2 shows no statistically significant associ-
331 ation (although the coefficients have the consistent sign).

332 The seasonal-level regressions show statistically significant anomalies only in Spring, when
333 positive Full SAM is associated with positive precipitation anomalies in Eastern Australia (panel
334 a.5). In this trimester the Symmetric SAM seems to be associated with precipitation in a relatively

reduced area of the East Coast (panel c.5) while the positive precipitation anomalies related with positive Asymmetric SAM affect all Eastern Australia (panel b.5).

In Summer, positive Full SAM index is associated with positive precipitation anomalies in Western and Eastern Australia, particularly in the North East (panel a.2). The Eastern part being dominated by the relationship with the Symmetric SAM and the Western, by the Asymmetric SAM. In Autumn, the regression with Full SAM shows positive values in the North, similar to Summer, and a broad area of positive values in the North-East to South-West direction. This structure seems to be associated with the Symmetric SAM, while the Northern positive values are associated with the Asymmetric SAM. In Winter we see the same NE to SW aligned anomaly (although with much reduced amplitude) that is also present only in relation with the Symmetric SAM. None of these regression coefficients are statistically significant at the 95% level

In South America (Figure 12), the annual-level regression shows that the SAM is associated with statistically significant precipitation decrease in Southeastern South America (SESA) and Southern Chile and non-significant increase in South Brazil, near the South Atlantic Convergence Zone (SACZ) (panel a.1). Panels b.1 and c.1 show a remarkably clean separation between the Asymmetric SAM –associated with the Southeastern South American and Southern Brazilian signals– and the Symmetric SAM –associated with the signal in Southern Chile.

Except Winter, seasonal-level regressions mirror this same pattern. Even if not statistically significant, they all show negative values in Southeastern South America and Southern Chile along with positive values in Southern Brazil in relation with the Full SAM. The separation of these features between the Asymmetric SAM and Symmetric SAM regression maps is also rather consistent.

The anomalous circulation at 700 hPa associated with the Symmetric SAM (panel c.1) indicate anomalous Easterly flow over Southern Chile. This leads to reduced influx of moist air from

the Pacific Ocean which, is the main source of precipitable water in that region. On the other hand, the anomalous circulation associated with positive values of Asymmetric SAM (panel b.1) in the Atlantic is anticyclonic in the South and cyclonic in the North. This creates anomalous South-Easterly flow over Southeastern South America, which inhibits the flow of the Low Level Jet to the region (Silvestri and Vera 2009; Zamboni et al. 2010). This same pattern was found to be associated with increased precipitation in Southern Brazil during South Atlantic Convergence Zone events (Rosso et al. 2018).

There is a small area of increased precipitation with SAM near central Argentina which is also present in the station-based analysis by Gillett et al. (2006) and that is explained by the Asymmetric SAM.

d. Conclusions

In this study we tried to systematically characterise the variability of the zonally symmetric and zonally asymmetric structure of the SAM. By projecting monthly geopotential fields at each level with the corresponding asymmetric and symmetric pattern, we created two indices representing the zonally asymmetric and zonally symmetric contributions of the SAM respectively.

As expected, the Asymmetric SAM index correlates strongly with the Symmetric SAM index. In the troposphere, this correlation is maximum at zero lag, while in the stratosphere is maximised with the Asymmetric SAM leading the Symmetric SAM by one month. Since most indices of the SAM are calculated using surface or near-surface conditions, this result would suggest that they might not be sensitive to the most dramatic changes in SAM variability.

The two-year periodicty we found in the stratospheric Symmetric SAM might point to a link between the SAM and the Quasi Biennial Oscillation. There is evidence of influence between the QBO and the Northern Annular Mode (e.g. Holton and Tan 1980; Watson and Gray 2014; Zhang

et al. 2020), so it's not unlikely that the SAM would be similarly connected. However establishing this link would require further research.

As documented by previous studies, such as Fogt and Marshall (2020) (and references therein), we observe a positive trend towards positive SAM in Summer and Autumn. We show that these trends are maximised at the 100 hPa level and are explained by the zonally symmetric component. We also find a statistically significant positive trend in the Symmetric component of the SAM in the stratosphere that is not apparent in the Full SAM index. In contrast to Fogt et al. (2012) we find some evidence of the SAM becoming more zonally asymmetric, as there is a slight positive trend in the variance explained by the as the Asymmetric SAM explains an increasingly proportion of the total variance.

In the troposphere, the spatial patterns of geopotential associated with the Symmetric SAM is much closer to being trully annular than the patterns associated with the Full SAM index. The Asymmetric SAM, on the other hand, describes a wave-3 pattern with maximum amplitude in the Pacific region and whose phae is rotated a quarter wavelength from the mean zonal wave 3 described by Raphael (2004)'s index. This pattern extends in the troposphere but its maximum is located at 250 hPa, which also could suggest that surface-based indices are not optimum for capturing this variability.

This wave-3 pattern is similar to the Pacific-South American Pattern, which is a teleconnection pattern linked to ENSO variability. We found that the significant correlation that exists between the Full SAM index and the Oceanic Niño Index is captured entirely by the Asymmetric SAM index. This suggests that ENSO is linked to SAM exclusively through the variability in the latter's Asymmetric compoment.

Temperature anomalies associated with the Full SAM broadly show a pattern of negative anomalies at polar latitudes surrounded by positive anomalies, but with many deviations from symmetry.

406 The Asymmetric SAM index explains a big portion of these deviations. In particular, the positive
407 phase of the Asymmetric SAM is associated with colder temperatures over Southern Brazil, South
408 Africa and Southern Australia, as well as the negative anomalies in the equatorial Pacific consis-
409 tent with the ENSO-SAM relationship delineated above. These are particularly clear in the DJF
410 and SON trimesters, which include the months in which the ENSO teleconnection is more active
411 (Cazes-Boezio et al. 2003; Fogt et al. 2011; Cai et al. 2020).

412 In Australia the Full SAM is associated with positive precipitation anomalies in South East and
413 this is explained by the Symmetric SAM. However, the Asymmetric SAM is associated with a
414 small area of positive precipitation anomalies in the Eastern Coast of West Australia, maybe due
415 to advection of moist air from the Indian Ocean.

416 In South America, precipitation anomalies associated with the Full SAM are negative both in
417 Southern Chile and Southeastern South America, and positive in Southern Brazil. This features
418 are cleanly separated between the Asymmetric and Symmetric components. The Symmetric SAM
419 explains the negative anomalies in Southern Chile and the Asymmetric SAM, the negative-positive
420 dipole between Southeastern South America and Southern Brazil. Individual seasons mostly follow
421 this pattern.

422 Silvestri and Vera (2009) suggests that precipitation impacts linked to the SAM changed rather
423 dramatically before and after 1980. In particular, the negative relationship with precipitation in
424 South America was absent in some areas and switched sign in other in the earlier period. The
425 correlation between ENSO and SAM is similarly non-stationary, also disappearing before 1973.

426 Seeing as both the ENSO-SAM relationship and most of the precipitation impacts in South
427 America are captured by the Asymmetric SAM, the results presented here are most likely period-
428 dependent. Therefore, is very likely that if we were to repeat this analysis using pre-satellite data,
429 the resulting Asymmetric SAM would look very different.

Acknowledgments. NOAA Global Surface Temperature (NOAAGlobalTemp) data provided by the NOAA/OAR/ESRL PSL, Boulder, Colorado, USA, from their Web site at <https://psl.noaa.gov/>

References

Baldwin, M. P., 2001: Annular modes in global daily surface pressure. *Geophysical Research Letters*, **28** (21), 4115–4118, doi:10.1029/2001GL013564.

Baldwin, M. P., and T. J. Dunkerton, 2001: Stratospheric Harbingers of Anomalous Weather Regimes. *Science*, **294** (5542), 581–584, doi:10.1126/science.1063315.

Baldwin, M. P., and D. W. J. Thompson, 2009: A critical comparison of stratosphere–troposphere coupling indices. *Quarterly Journal of the Royal Meteorological Society*, **135** (644), 1661–1672, doi:10.1002/qj.479.

Bamston, A. G., M. Chelliah, and S. B. Goldenberg, 1997: Documentation of a highly ENSO-related sst region in the equatorial pacific: Research note. *Atmosphere-Ocean*, **35** (3), 367–383, doi:10.1080/07055900.1997.9649597.

Benjamini, Y., and Y. Hochberg, 1995: Controlling the False Discovery Rate: A Practical and Powerful Approach to Multiple Testing. *Journal of the Royal Statistical Society: Series B (Methodological)*, **57** (1), 289–300, doi:10.1111/j.2517-6161.1995.tb02031.x.

Cai, W., and Coauthors, 2020: Climate impacts of the El Niño–Southern Oscillation on South America. *Nature Reviews Earth & Environment*, **1** (4), 215–231, doi:10.1038/s43017-020-0040-3.

Cazes-Boezio, G., A. W. Robertson, and C. R. Mechoso, 2003: Seasonal Dependence of ENSO Teleconnections over South America and Relationships with Precipitation in Uruguay. *J. Climate*, **16** (8), 1159–1176, doi:10.1175/1520-0442(2003)16<1159:SDOETO>2.0.CO;2.

- 452 Chung, C., and S. Nigam, 1999: Weighting of geophysical data in Principal Component
453 Analysis. *Journal of Geophysical Research: Atmospheres*, **104 (D14)**, 16 925–16 928, doi:
454 10.1029/1999JD900234.
- 455 Clem, K. R., and R. L. Fogt, 2013: Varying roles of ENSO and SAM on the Antarctic Peninsula
456 climate in austral spring. *Journal of Geophysical Research: Atmospheres*, **118 (20)**, 11,481–
457 11,492, doi:10.1002/jgrd.50860.
- 458 Fan, K., 2007: Zonal asymmetry of the Antarctic Oscillation. *Geophysical Research Letters*, **34 (2)**,
459 doi:10.1029/2006GL028045.
- 460 Fogt, R. L., and D. H. Bromwich, 2006: Decadal Variability of the ENSO Teleconnection to
461 the High-Latitude South Pacific Governed by Coupling with the Southern Annular Mode. *J.*
462 *Climate*, **19 (6)**, 979–997, doi:10.1175/JCLI3671.1.
- 463 Fogt, R. L., D. H. Bromwich, and K. M. Hines, 2011: Understanding the SAM influ-
464 ence on the South Pacific ENSO teleconnection. *Clim Dyn*, **36 (7)**, 1555–1576, doi:
465 10.1007/s00382-010-0905-0.
- 466 Fogt, R. L., J. M. Jones, and J. Renwick, 2012: Seasonal Zonal Asymmetries in the Southern
467 Annular Mode and Their Impact on Regional Temperature Anomalies. *J. Climate*, **25 (18)**,
468 6253–6270, doi:10.1175/JCLI-D-11-00474.1.
- 469 Fogt, R. L., and G. J. Marshall, 2020: The Southern Annular Mode: Variability, trends, and
470 climate impacts across the Southern Hemisphere. *WIREs Climate Change*, **11 (4)**, e652, doi:
471 10.1002/wcc.652.
- 472 Gillett, N. P., T. D. Kell, and P. D. Jones, 2006: Regional climate impacts of the Southern Annular
473 Mode. *Geophysical Research Letters*, **33 (23)**, doi:10.1029/2006GL027721.

- Gong, D., and S. Wang, 1999: Definition of Antarctic Oscillation index. *Geophysical Research Letters*, **26** (4), 459–462, doi:10.1029/1999GL900003.
- Hendon, H. H., D. W. J. Thompson, and M. C. Wheeler, 2007: Australian Rainfall and Surface Temperature Variations Associated with the Southern Hemisphere Annular Mode. *J. Climate*, **20** (11), 2452–2467, doi:10.1175/JCLI4134.1.
- Hersbach, H., and Coauthors, 2020: The ERA5 global reanalysis. *Quarterly Journal of the Royal Meteorological Society*, **146** (730), 1999–2049, doi:10.1002/qj.3803.
- Ho, M., A. S. Kiem, and D. C. Verdon-Kidd, 2012: The Southern Annular Mode: A comparison of indices. *Hydrology and Earth System Sciences*, **16** (3), 967–982, doi:10.5194/hess-16-967-2012.
- Holton, J. R., and H.-C. Tan, 1980: The Influence of the Equatorial Quasi-Biennial Oscillation on the Global Circulation at 50 mb. *J. Atmos. Sci.*, **37** (10), 2200–2208, doi:10.1175/1520-0469(1980)037<2200:TIOTEQ>2.0.CO;2.
- Jones, J. M., R. L. Fogg, M. Widmann, G. J. Marshall, P. D. Jones, and M. Visbeck, 2009: Historical SAM Variability. Part I: Century-Length Seasonal Reconstructions. *J. Climate*, **22** (20), 5319–5345, doi:10.1175/2009JCLI2785.1.
- Jones, M. E., D. H. Bromwich, J. P. Nicolas, J. Carrasco, E. Plavcová, X. Zou, and S.-H. Wang, 2019: Sixty Years of Widespread Warming in the Southern Middle and High Latitudes (1957–2016). *J. Climate*, **32** (20), 6875–6898, doi:10.1175/JCLI-D-18-0565.1.
- Karoly, D. J., 1989: Southern Hemisphere Circulation Features Associated with El Niño–Southern Oscillation Events. *J. Climate*, **2** (11), 1239–1252, doi:10.1175/1520-0442(1989)002<1239:SHCFAW>2.0.CO;2.

495 Katz, R. W., and B. G. Brown, 1991: The problem of multiplicity in research on teleconnections.
 496 *International Journal of Climatology*, **11** (5), 505–513, doi:10.1002/joc.3370110504.

497 Kidson, J. W., 1988: Interannual Variations in the Southern Hemisphere Circulation. *J. Climate*,
 498 **1** (12), 1177–1198, doi:10.1175/1520-0442(1988)001<1177:IVITSH>2.0.CO;2.

499 Lim, E.-P., H. H. Hendon, J. M. Arblaster, F. Delage, H. Nguyen, S.-K. Min, and M. C. Wheeler,
 500 2016: The impact of the Southern Annular Mode on future changes in Southern Hemisphere
 501 rainfall. *Geophysical Research Letters*, **43** (13), 7160–7167, doi:10.1002/2016GL069453.

502 Marshall, G. J., 2003: Trends in the Southern Annular Mode from Observations and Reanalyses.
 503 *J. Climate*, **16** (24), 4134–4143, doi:10.1175/1520-0442(2003)016<4134:TITSAM>2.0.CO;2.

504 Mo, K. C., and M. Ghil, 1987: Statistics and Dynamics of Persistent Anomalies. *J. Atmos. Sci.*,
 505 **44** (5), 877–902, doi:10.1175/1520-0469(1987)044<0877:SADOPA>2.0.CO;2.

506 Raphael, M. N., 2004: A zonal wave 3 index for the Southern Hemisphere. *Geophysical Research*
 507 *Letters*, **31** (23), doi:10.1029/2004GL020365.

508 Rogers, J. C., and H. van Loon, 1982: Spatial Variability of Sea Level Pressure and 500 mb
 509 Height Anomalies over the Southern Hemisphere. *Mon. Wea. Rev.*, **110** (10), 1375–1392, doi:
 510 10.1175/1520-0493(1982)110<1375:SVOSLP>2.0.CO;2.

511 Ropelewski, C. F., and P. D. Jones, 1987: An Extension of the Tahiti–Darwin Southern Oscil-
 512 lation Index. *Mon. Wea. Rev.*, **115** (9), 2161–2165, doi:10.1175/1520-0493(1987)115<2161:
 513 AEOTTS>2.0.CO;2.

514 Rosso, F. V., N. T. Boiaski, S. E. T. Ferraz, and T. C. Robles, 2018: Influence of the Antarctic
 515 Oscillation on the South Atlantic Convergence Zone. *Atmosphere*, **9** (11), 431, doi:10.3390/
 516 atmos9110431.

517 Schneider, U., A. Becker, P. Finger, A. Meyer-Christoffer, B. Rudolf, and M. Ziese, 2015: GPCC
 518 Full Data Reanalysis Version 7.0 at 0.5°: Monthly Land-Surface Precipitation from Rain-Gauges
 519 built on GTS-based and Historic Data: Gridded Monthly Totals. Global Precipitation Clima-
 520 tology Centre (GPCC) at Deutscher Wetterdienst, 20 - 270 MB per decadal gzip compressed
 521 NetCDF archive pp., doi:10.5676/DWD_GPCC/FD_M_V7_050.

522 Silvestri, G., and C. Vera, 2009: Nonstationary Impacts of the Southern Annular Mode on Southern
 523 Hemisphere Climate. *J. Climate*, **22** (22), 6142–6148, doi:10.1175/2009JCLI3036.1.

524 Smith, T. M., R. W. Reynolds, T. C. Peterson, and J. Lawrimore, 2008: Improvements to NOAA’s
 525 Historical Merged Land–Ocean Surface Temperature Analysis (1880–2006). *J. Climate*, **21** (10),
 526 2283–2296, doi:10.1175/2007JCLI2100.1.

527 Vose, R. S., and Coauthors, 2012: NOAA’s Merged Land–Ocean Surface Temperature Analysis.
 528 *Bull. Amer. Meteor. Soc.*, **93** (11), 1677–1685, doi:10.1175/BAMS-D-11-00241.1.

529 Walker, S. G. T., 1914: *Correlation in Seasonal Variations of Weather, III: On the Criterion for*
 530 *the Reality of Relationships Or Periodicities*. Meteorological Office.

531 Watson, P. A. G., and L. J. Gray, 2014: How Does the Quasi-Biennial Oscillation Affect the
 532 Stratospheric Polar Vortex? *J. Atmos. Sci.*, **71** (1), 391–409, doi:10.1175/JAS-D-13-096.1.

533 Wilks, D. S., 2016: “The Stippling Shows Statistically Significant Grid Points”: How Research
 534 Results are Routinely Overstated and Overinterpreted, and What to Do about It. *Bull. Amer.*
 535 *Meteor. Soc.*, **97** (12), 2263–2273, doi:10.1175/BAMS-D-15-00267.1.

536 Wolter, K., and M. S. Timlin, 2011: El Niño/Southern Oscillation behaviour since 1871 as diag-
 537 nosed in an extended multivariate ENSO index (MEI.ext). *International Journal of Climatology*,
 538 **31** (7), 1074–1087, doi:10.1002/joc.2336.

539 Zamboni, L., C. R. Mechoso, and F. Kucharski, 2010: Relationships between Upper-Level Circu-
540 lation over South America and Rainfall over Southeastern South America: A Physical Base for
541 Seasonal Predictions. *J. Climate*, **23** (12), 3300–3315, doi:10.1175/2009JCLI3129.1.

542 Zhang, R., W. Tian, and T. Wang, 2020: Role of the quasi-biennial oscillation in the downward
543 extension of stratospheric northern annular mode anomalies. *Clim Dyn*, **55** (3), 595–612, doi:
544 10.1007/s00382-020-05285-4.

545

APPENDIX

546

Extra figures

547	LIST OF FIGURES	
548	Fig. 1. Spatial patterns of the first EOF of 700 hPa geopotential height	30
549	Fig. 2. Time series for the Asymmetric SAM and Symmetric SAM indices at (a) 50 hPa and (b) 700	
550	hPa	31
551	Fig. 3. Correlation between the Symmetric SAM and Asymmetric SAM index at each level for lag	
552	zero and lag -1 (Symmetric leads Asymmetric)	32
553	Fig. 4. Cross correlation between levels of the (a) Full SAM, (b) Asymmetric SAM, and (c) Sym-	
554	metric SAM	33
555	Fig. 5. Decadal trends at each level for annual (row 1) and seasonal values (rows 2 to 5) for the	
556	period 1979-2018 and for the (column a) Full SAM index, (column b) Asymmetric SAM	
557	index, and (column c) Symmetric SAM index	34
558	Fig. 6. Decadal trends of the variance explained by the Asymmetric and Symmetric SAM at each	
559	level for the period 1979-2018	35
560	Fig. 7. Regression patterns of geopotential height (meters) at (row 1) 50 hPa and (row 2) 700 hPa	
561	with the (column a) Full SAM, (column b) Asymmetric SAM, and (column c) Symmetric	
562	SAM	36
563	Fig. 8. Amplitude (meters) of zonal waves of the geopotential height regression patterns in Figure	
564	7 for zonal waves with wave-number 0, 1, 2, and 3, where wave-number 0 represents the	
565	amplitude of the zonal mean. Note the different x axis.	37
566	Fig. 9. Regression between monthly geopotential anomalies (meters) averaged between 65° and	
567	40°S and the Asymmetric SAM index (extracted from multiple regression including the	
568	Symmetric SAM)	38
569	Fig. 10. Regression pattern of season mean surface temperature (Kelvin) with Asymmetric SAM and	
570	Symmetric SAM	39
571	Fig. 11. Regression pattern of (row 1) annual and (rows 2 to 5) season mean precipitation anomalies	
572	(mm per day, shading) and 700 hPa geopotential height (thin lines, positive values as solid	
573	lines and negative values as dashed lines) with (column a) Full SAM, (column b) Asymmetric	
574	SAM and (column c) Symmetric SAM	40
575	Fig. 12. Same as Figure 11 but for South America.	41
576	Fig. A1. Lag-correlation between Asymmetric SAM and Symmetric SAM index at each level. Neg-	
577	ative lags imply Symmetric SAM leading Asymmetric SAM and vice versa.	42
578	Fig. A3. Fourier spectrum of each timeseries computed as Fourier transform smoothed with modified	
579	Daniell smoothers with widths 3 and 5. The shading indicates the 95% confidence area derived	
580	by fitting an autoregressive model and computing the spectrum for 5000 simulated samples	
581	from the fitted autoregressive model (95% of the simulated samples had an amplitude equal	
582	or lower). The light line indicates the theoretical expected amplitude from the autoregressive	
583	model.	43

584	Fig. 13.	700 hPa Geopotetnial height zonal anomalies (meters) of composites of positive and negative	
585		SAM months selected using ± 1 standard deviation as threshhld	44
586	Fig. 14.	Regression of 700 hPa geopotential height zonal anomalies (meters) onto the standarised	
587		timeseries of the leading EOF computed for each season independently	45
588	Fig. 15.	Regression of 700 hPa geopotential height zonal anomalies (meters) onto the standarised	
589		timeseries of the leading EOF computed for the periods 1979 to 1998 and 1999 to 2018	46

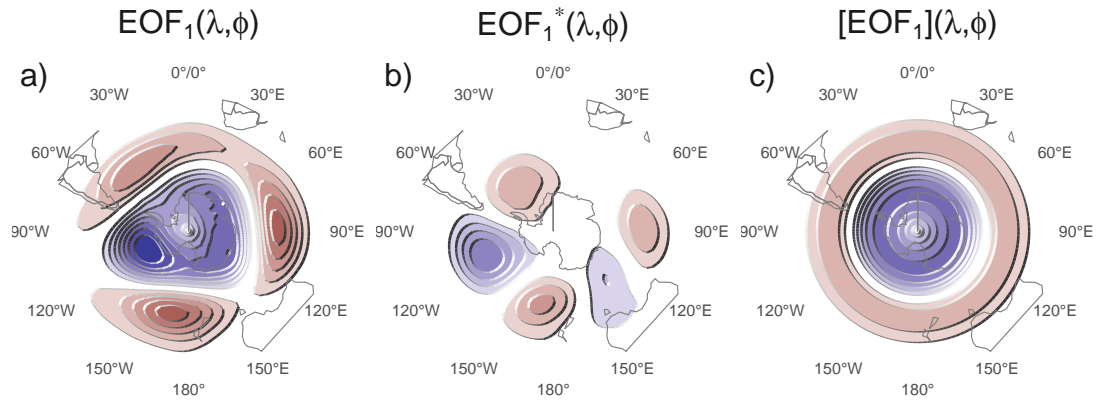


FIG. 1: Spatial patterns of the first EOF of 700 hPa geopotential height. (a) Full field, (b) zonally asymmetric component and (c) zonally symmetric component. Arbitrary units.

fig:method

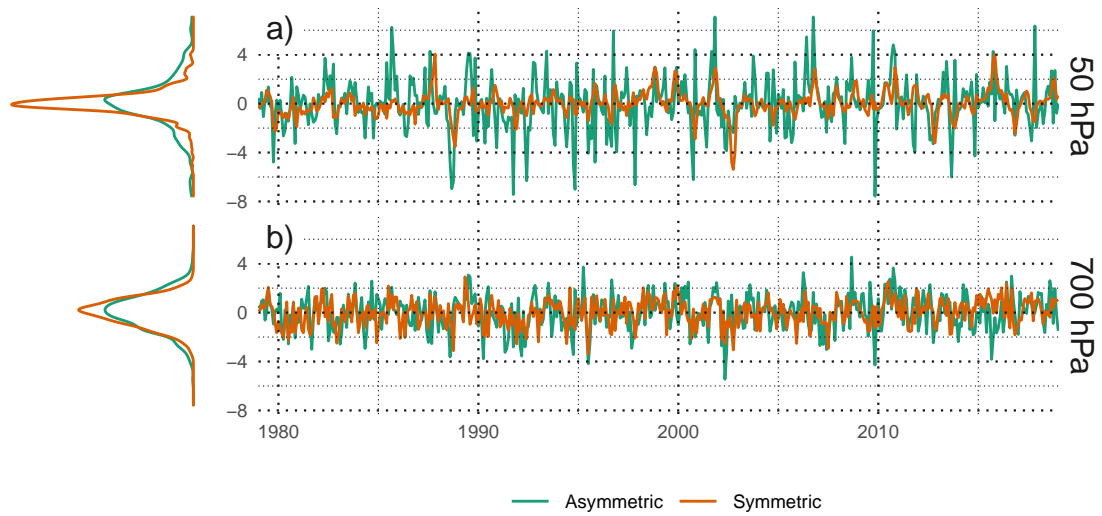


FIG. 2: Time series for the Asymmetric SAM and Symmetric SAM indices at (a) 50 hPa and (b) 700 hPa. To the left, probability density estimate of each index. Series are standardised by the standard deviation of the Full SAM at each level.

fig:asysam-timeseries

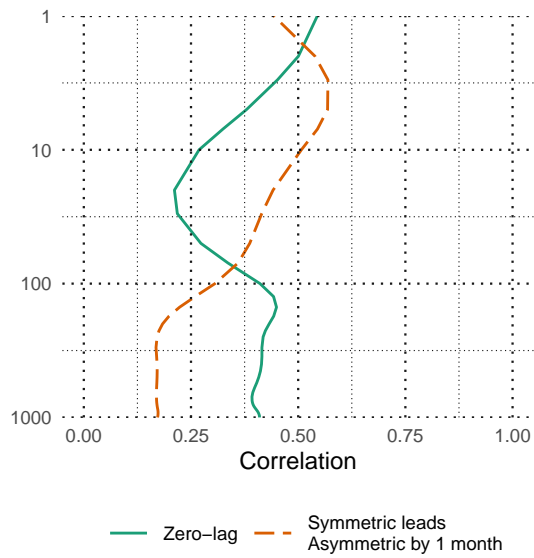


FIG. 3: Correlation between the Symmetric SAM and Asymmetric SAM index at each level for lag zero and lag -1 (Symmetric leads Asymmetric).

fig:cor-lev

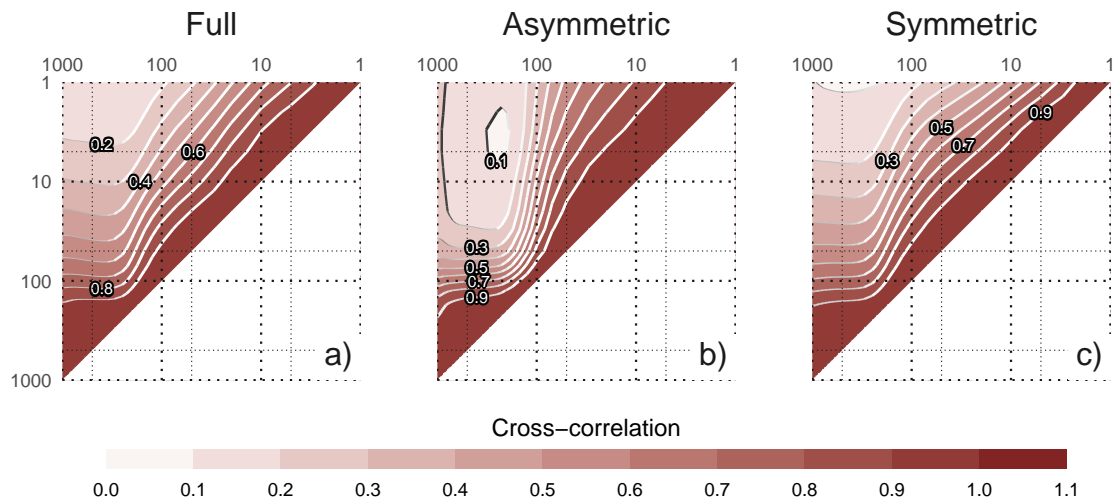


FIG. 4: Cross correlation between levels of the (a) Full SAM, (b) Asymmetric SAM, and (c) Symmetric SAM.

fig:cross-correlation

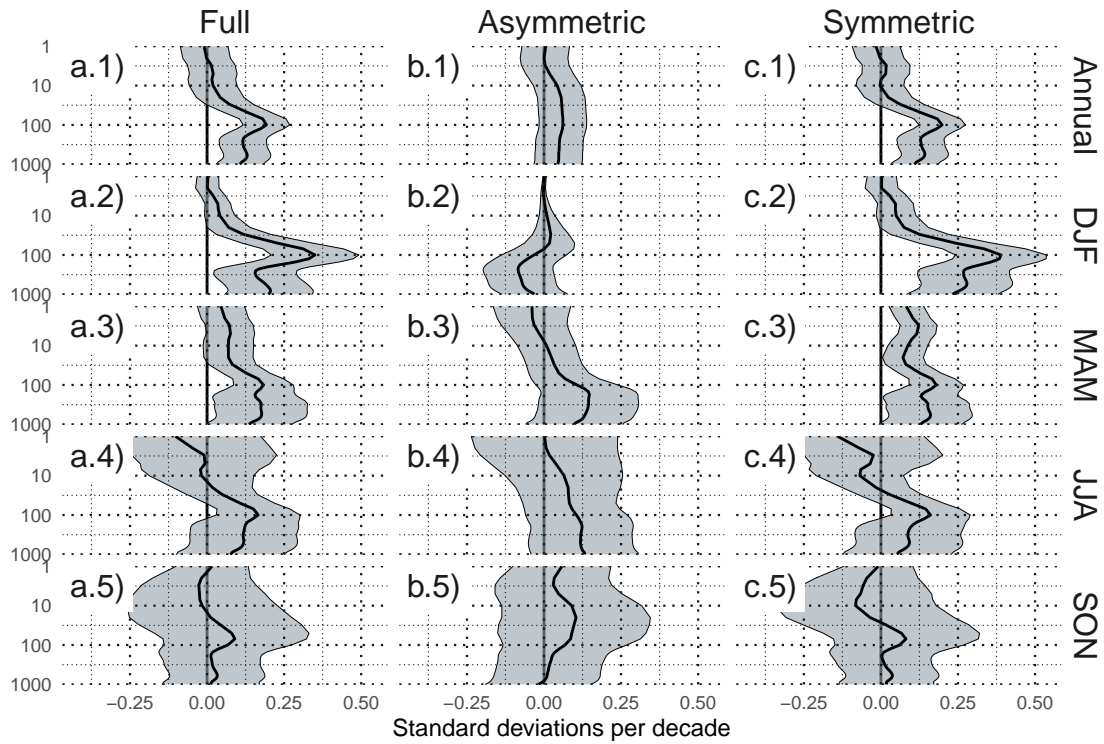


FIG. 5: Decadal trends at each level for annual (row 1) and seasonal values (rows 2 to 5) for the period 1979-2018 and for the (column a) Full SAM index, (column b) Asymmetric SAM index, and (column c) Symmetric SAM index. Shading indicates the 95% confidence interval.

fig:trends

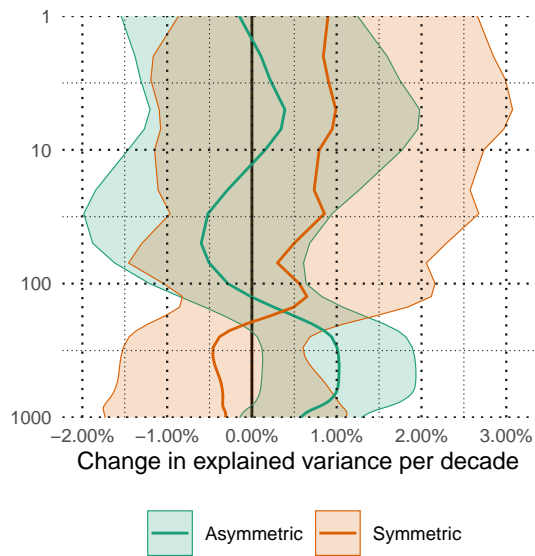


FIG. 6: Decadal trends of the variance explained by the Asymmetric and Symmetric SAM at each level for the period 1979-2018. Shading indicates the 95% confidence interval.

fig:r-squared-trend

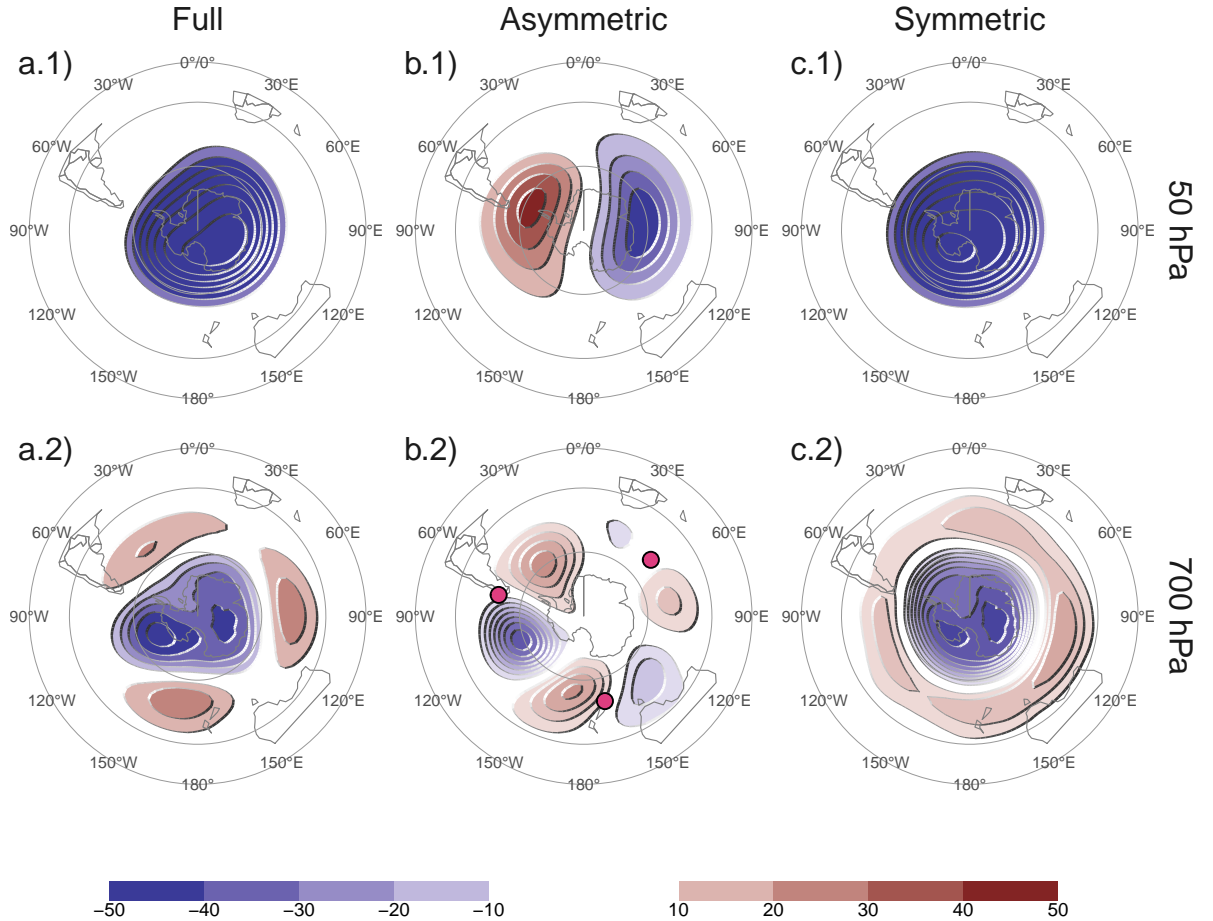


FIG. 7: Regression patterns of geopotential height (meters) at (row 1) 50 hPa and (row 2) 700 hPa with the (column a) Full SAM, (column b) Asymmetric SAM, and (column c) Symmetric SAM. The regression patterns for Asymmetric and Symmetric SAM are the result of one multiple regression using both indices, not of two simple regressions involving each index by itself. Points marked on panel b.2 are the location of the reference points used by Raphael (2004) for their Zonal Wave 3 index.

fig:2d-regr

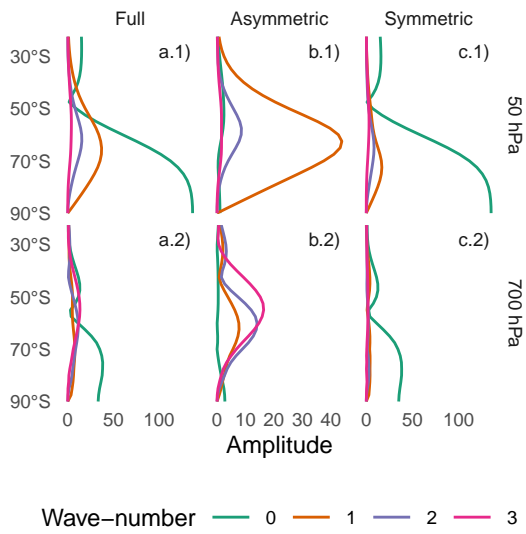


FIG. 8: Amplitude (meters) of zonal waves of the geopotential height regression patterns in Figure 7 for zonal waves with wave-number 0, 1, 2, and 3, where wave-number 0 represents the amplitude of the zonal mean. Note the different x axis.

fig:wave-amplitude

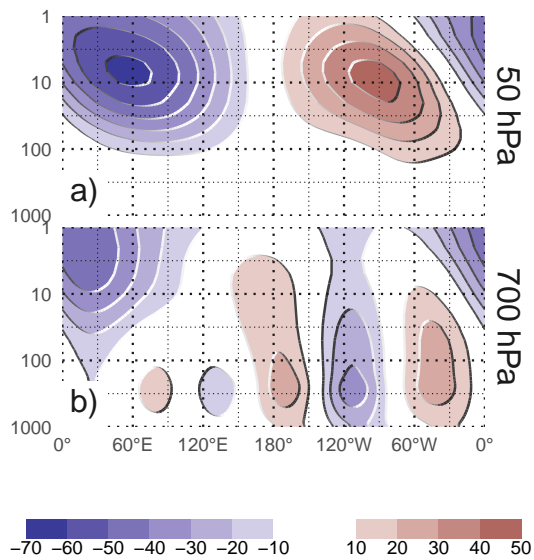


FIG. 9: Regression between monthly geopotential anomalies (meters) averaged between 65° and 40°S and the Asymmetric SAM index (extracted from multiple regression including the Symmetric SAM). (a) With the Asymmetric SAM in 50 hPa and (b) in 700 hPa.

fig:vertical-regression

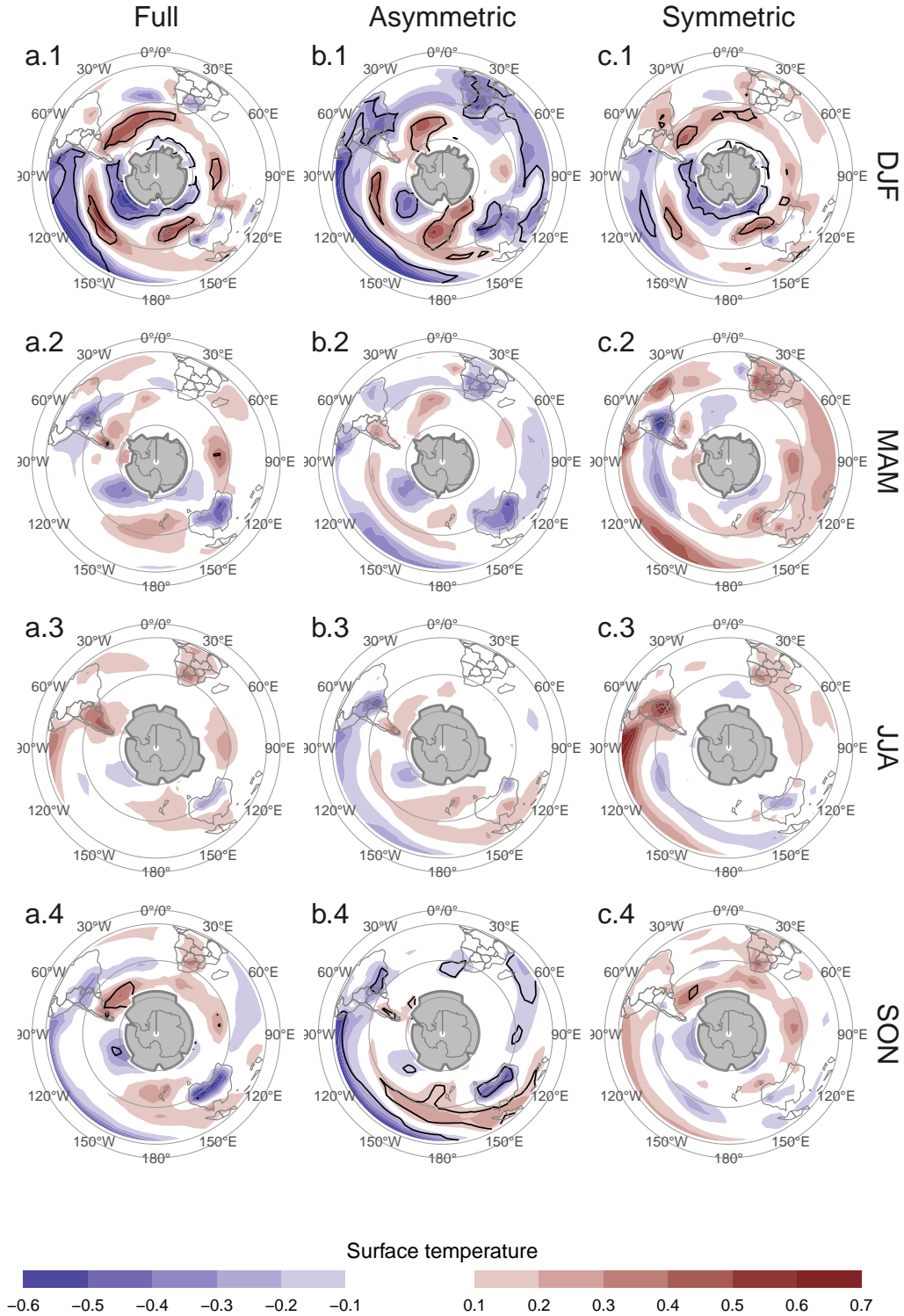


FIG. 10: Regression pattern of season mean surface temperature (Kelvin) with Asymmetric SAM and Symmetric SAM. Black contours indicate areas with p-value smaller than 0.05 controlling for False Detection Rate. Gray areas in Antarctica are areas with have more than 15% of missing data.
fig:regr-air-season

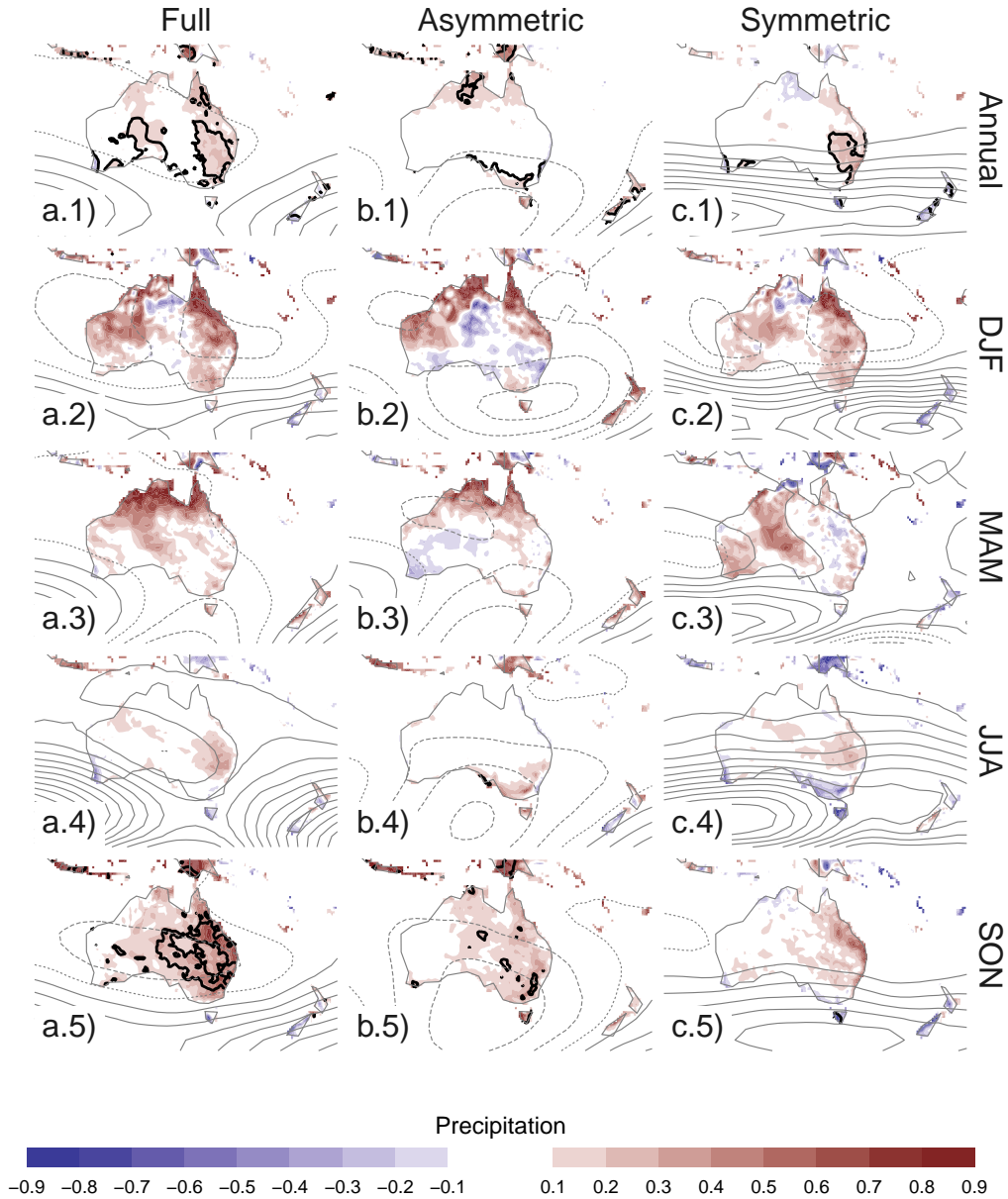


FIG. 11: Regression pattern of (row 1) annual and (rows 2 to 5) season mean precipitation anomalies (mm per day, shading) and 700 hPa geopotential height (thin lines, positive values as solid lines and negative values as dashed lines) with (column a) Full SAM, (column b) Asymmetric SAM and (column c) Symmetric SAM. thin lines are the Black contours indicate areas with p-value smaller than 0.05 controlling for False Detection Rate.

fig:pp-regr-oceania

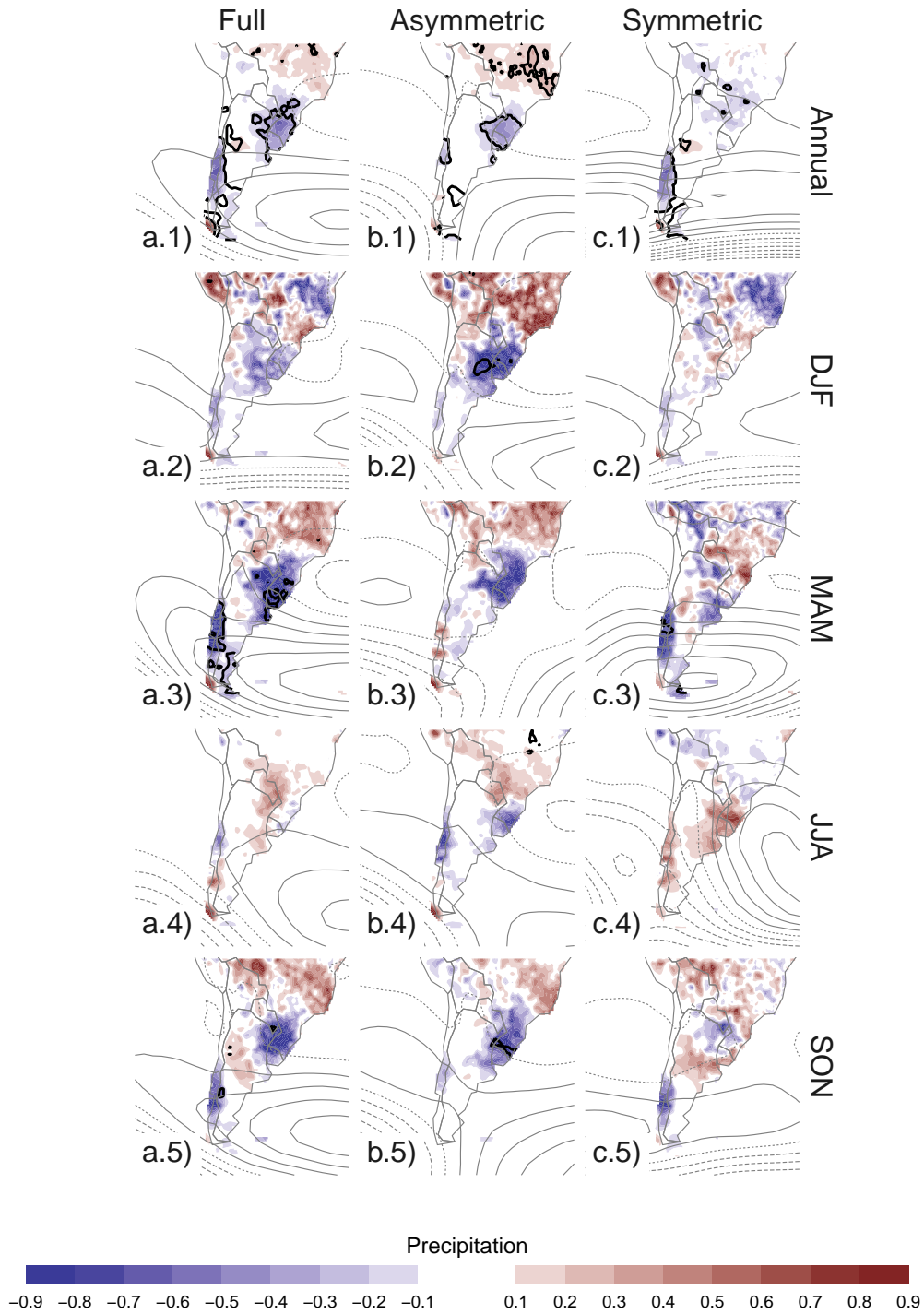


FIG. 12: Same as Figure 11 but for South America.

fig:pp-regr-america

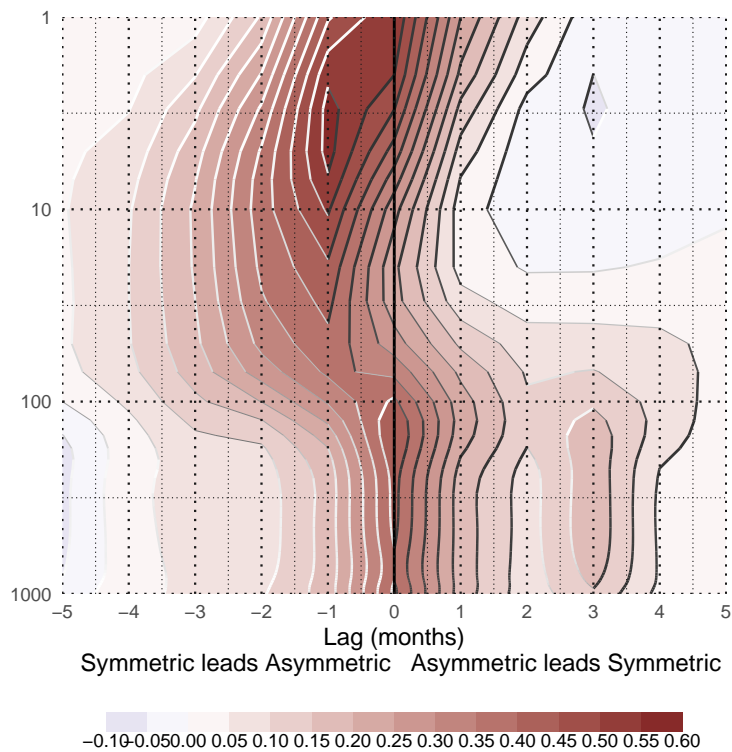


Fig. A1: Lag-correlation between Asymmetric SAM and Symmetric SAM index at each level. Negative lags imply Symmetric SAM leading Asymmetric SAM and vice versa.

fig:A1

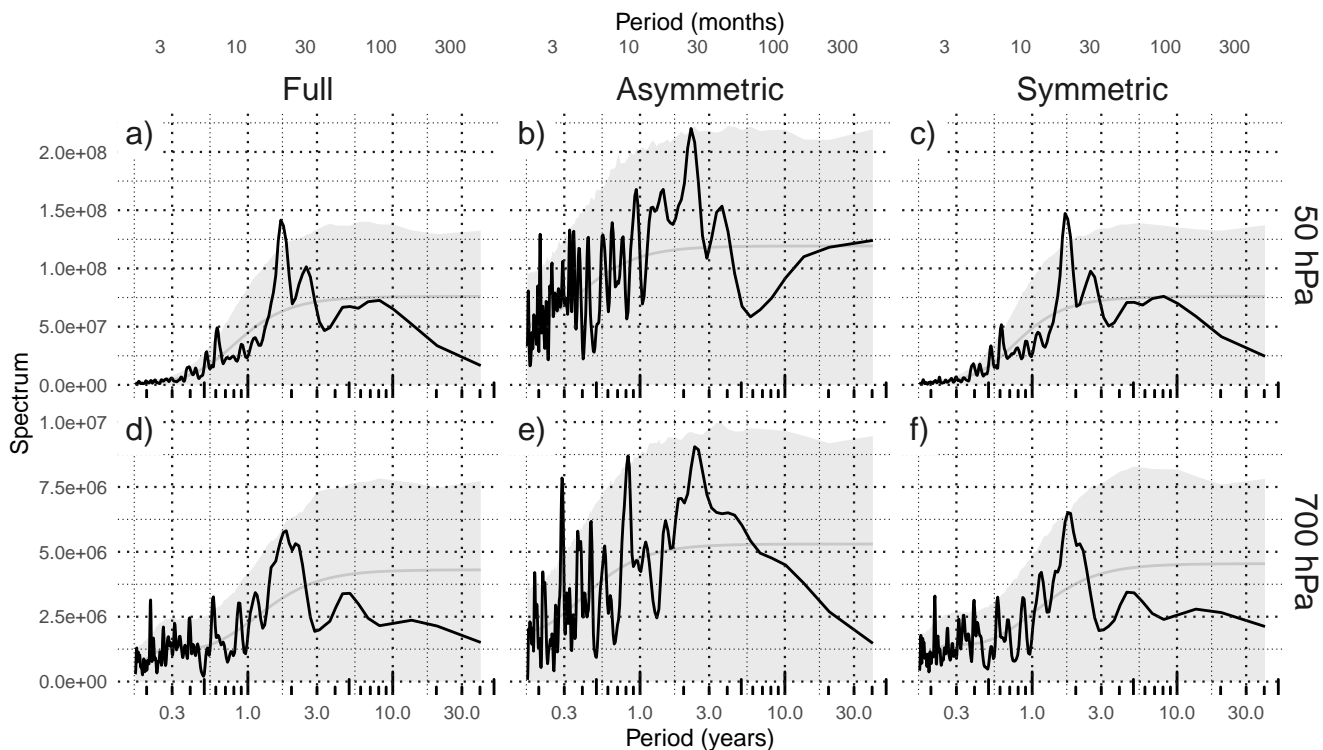


Fig. A3: Fourier spectrum of each timeseries computed as Fourier transform smoothed with modified Daniell smoothers with withs 3 and 5. The shading indicates de 95% confidence area derived by fitting an autorregressive model and computing the spectrum for 5000 simulated samples from the fitted autorregressive model (95% of the simulated sampels had an amplitude equal or lower). The light line indicates the theorethical expected amplitude from the autorregressive model.

fig:A3

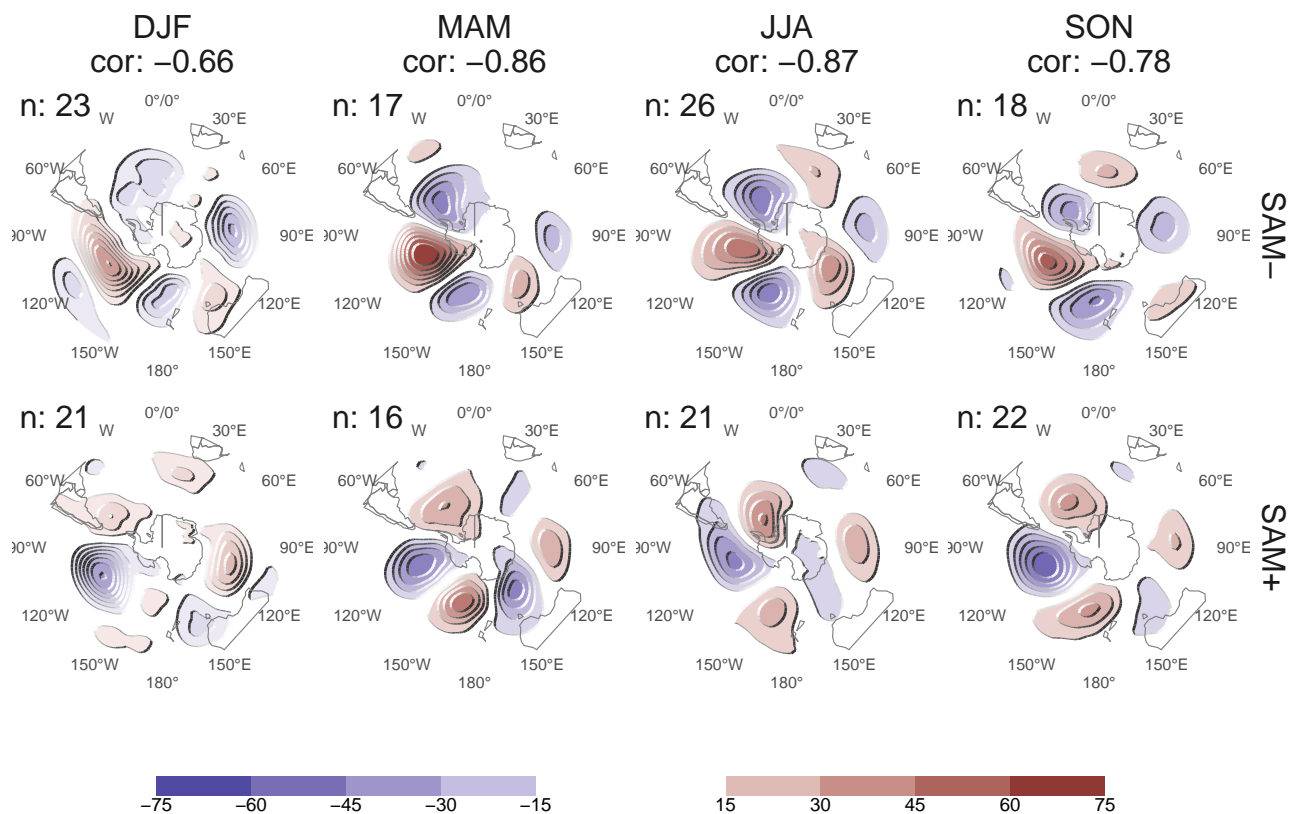


FIG. 13: 700 hPa Geopotential height zonal anomalies (meters) of composites of positive and negative SAM months selected using ± 1 standard deviation as threshold. Numbers in the column headers are pattern correlation between SAM+ and SAM- composites and number of monthly fields used to construct the composites.

fig:A9

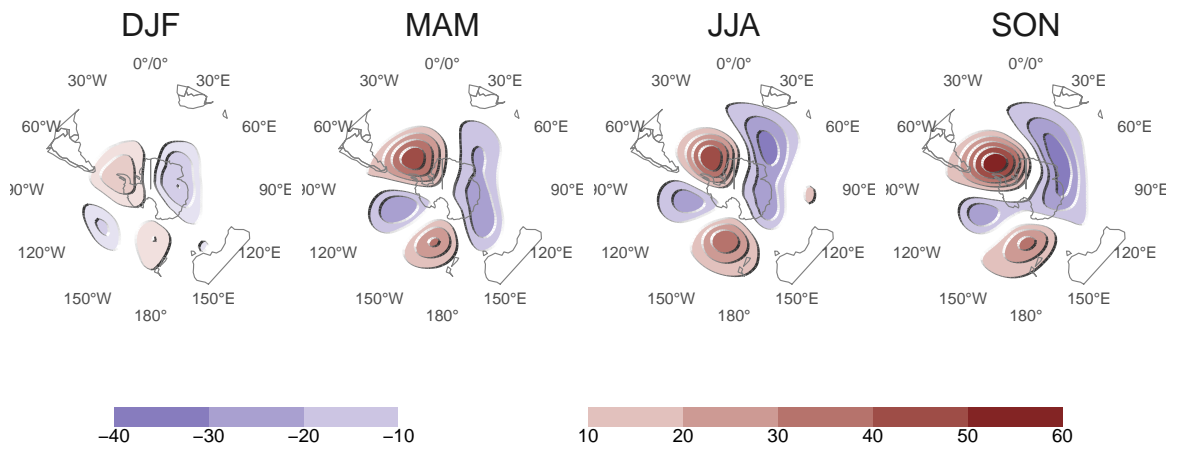


FIG. 14: Regression of 700 hPa geopotential height zonal anomalies (meters) onto the standardised timeseries of the leading EOF computed for each season independently.

fig:A10

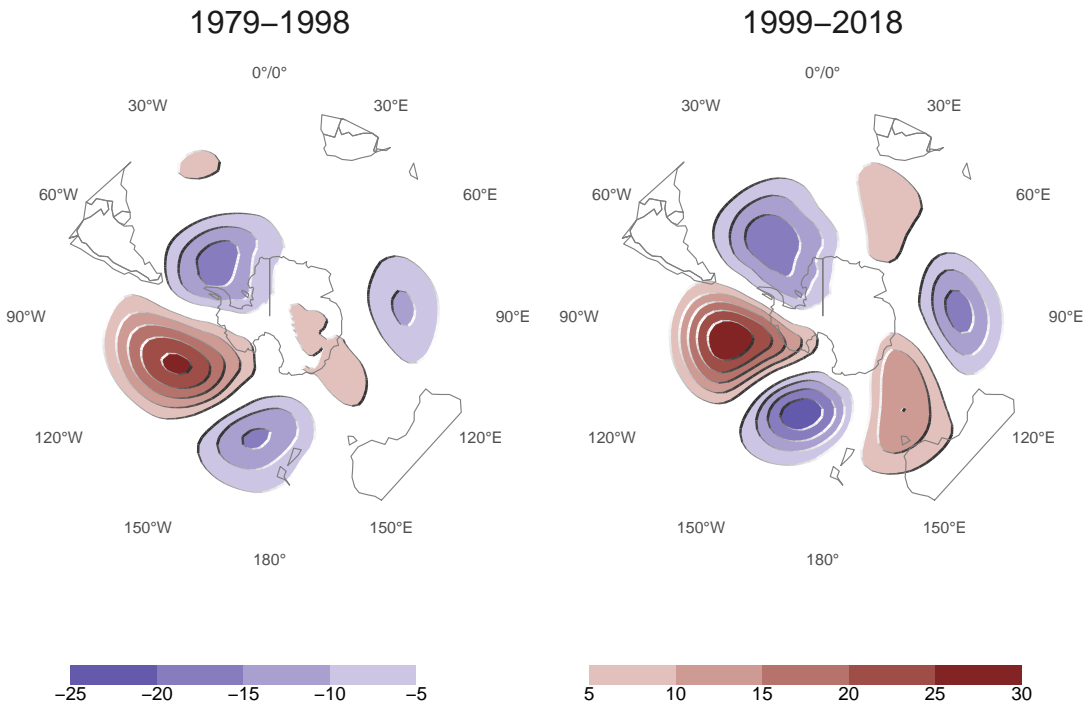


FIG. 15: Regression of 700 hPa geopotential height zonal anomalies (meters) onto the standardised timeseries of the leading EOF computed for the periods 1979 to 1998 and 1999 to 2018. Pattern correlation between both fields is 0.76.

fig:A11